Perovskite solar cells with a planar heterojunction structure prepared using room-temperature solution processing techniques

Dianyi Liu and Timothy L. Kelly*

Organic–inorganic hybrid solar cells that combine a mesoporous scaffold, a perovskite light absorber and an organic hole transporter have emerged at the forefront of solution-processable photovoltaic devices; however, they require processing temperatures of up to 500 °C to sinter the mesoporous metal-oxide support. Here, we report the use of a thin film of ZnO nanoparticles as an electron-transport layer in CH$_3$NH$_3$PbI$_3$-based solar cells; in contrast to mesoporous TiO$_2$, the ZnO layer is both substantially thinner and requires no sintering. We took advantage of these facts to prepare flexible solar cells with power-conversion efficiencies in excess of 10%. The use of ZnO also results in improvements to device performance for cells prepared on rigid substrates. Solar cells based on this design exhibit power-conversion efficiencies as high as 15.7% when measured under AM1.5G illumination, which makes them some of the highest-performing perovskite solar cells reported to date.

Research in the area of solution-processable solar cells has led to substantial progress in the development of both organic and hybrid photovoltaic devices, with power-conversion efficiencies (PCEs) now routinely approaching or exceeding 10%. This progress has been driven by the synthesis of new electron-donor materials (both polymers and small-molecule chromophores) for organic photovoltaic (OPV) devices[1–3], and the preparation of new dyes and redox mediators for dye-sensitized solar cells (DSSCs)[4,5]. Despite these advances, the efficiencies of both OPV and DSSC devices are inherently limited by losses associated with the thermodynamic driving force required to either dissociate a strongly bound exciton or drive electron-transfer processes in a DSSC. One exciting alternative to these traditional device architectures is the hybrid organic–inorganic devices that utilize perovskite-based materials as the light-absorbing component[6]. Early work utilized very small CH$_3$NH$_3$PbI$_3$ nanoparticles to sensitize TiO$_2$, and produced PCEs of 3–4%[7]; however, since then advances in cell design have led to remarkably rapid improvements in device efficiency[8–20]. State-of-the-art perovskite solar cells based on a mesoporous titanium dioxide scaffold, a CH$_3$NH$_3$PbI$_3$ light-absorption layer and a 2,2′,7,7′-tetrakis-(N,N-di-p-methoxyphenylamine)-9,9′-bifluorene (spiro-OMeTAD) hole transport layer have achieved PCEs as high as 15.0%[21], and several reports suggest that solar cells with efficiencies up to 20% are realistically achievable[6,22].

Currently, most state-of-the-art perovskite-based devices utilize a mesoporous metal-oxide scaffold to provide a porous substrate on which the CH$_3$NH$_3$PbI$_3$ light absorber can be grown. In addition to acting as a structure-directing support, the titania scaffolds are also responsible for accepting electrons from the absorber and transporting them to the electrode surface[20,21]. Although relatively thin compared to the mesoporous TiO$_2$ films traditionally used in liquid electrolyte DSSCs (350 nm versus ∼10 μm in a traditional DSSC), these layers are, nonetheless, substantially thicker than the electron-transport layers typically utilized in inverted OPV devices (40 nm)[23,24]; in addition, the mesoporous films require sintering at 450–550 °C prior to use, which renders them incompatible with flexible substrates. Recently, Snaith and co-workers demonstrated

that the high efficiency of perovskite-based devices could be maintained or further improved by replacing the titania mesoporous scaffold with an insulating Al$_2$O$_3$ analogue[25,26], and that the Al$_2$O$_3$ matrix could be constructed at lower temperatures (110–150 °C) than those required for mesoporous TiO$_2$ (refs 27,28). Further work has demonstrated that perovskite solar cells with up to 15.4% efficiency can be produced in the absence of a mesoporous matrix by a vapour-phase deposition process[29], and efficiencies up to 11.4% have been achieved using solution-phase approaches[30]. Motivated by the desire to simplify further the processing of these perovskite-based solar cells, we investigated the use of a relatively compact electron-transport layer based on ZnO nanoparticles as an alternative to both the mesoporous TiO$_2$ (ref. 21) and Al$_2$O$_3$ (ref. 25) scaffolds and vapour-phase deposition approaches[29] reported previously. ZnO is known to have an electron mobility that is substantially higher than that of TiO$_2$ (ref. 31), which makes it an ideal choice for an electron-selective contact. Additionally, the ZnO nanoparticle layer can be deposited easily by spin coating and requires no heating or sintering step, which makes it ideal for deposition on thermally sensitive substrates. Devices based on this design performed extremely well, with PCEs reaching 15.7% when illuminated and tested under standard AM1.5G conditions. Flexible devices could also be prepared by this method, and displayed PCEs over 10%. The solution-processing of the ZnO layer is simple, economical and proceeds at room temperature, which gives it important advantages over other cell designs that use mesoporous scaffolds[21,25] or vapour-phase deposition techniques[29].

The ZnO nanoparticles used in the fabrication of the electron-selective contacts were prepared by the hydrolysis of zinc acetate in methanol[32,33]. This process produces crystalline nanoparticles that are approximately 5 nm in diameter, as determined by transmission electron microscopy (TEM; Supplementary Fig. 1). The nanoparticles are dispersed readily in butanol/chloroform mixtures with no additional surfactants or binders; as such, after they are spin coated onto the indium tin oxide (ITO) substrate, no calcination or sintering step is required. This process produces a relatively compact ZnO layer,
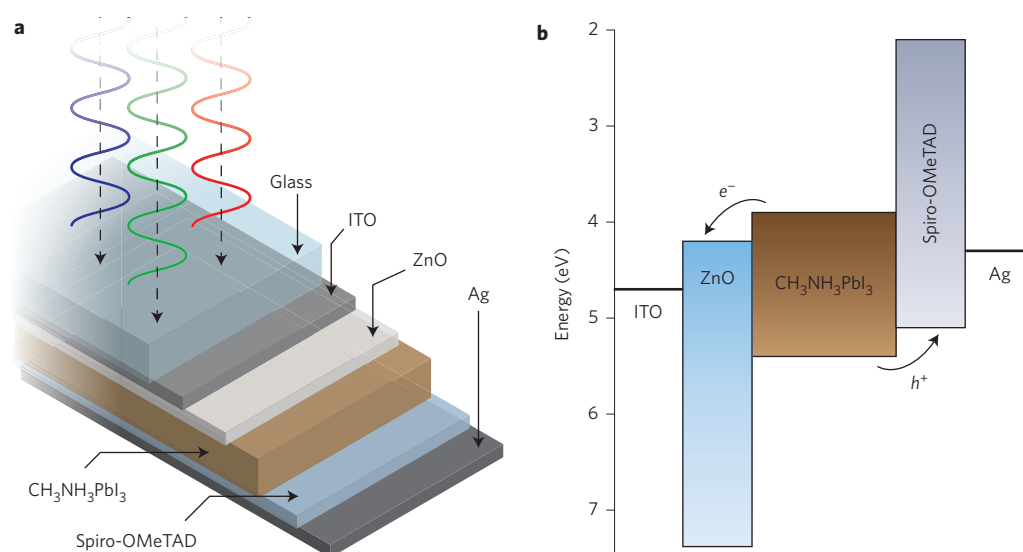
Department of Chemistry, University of Saskatchewan, 110 Science Place, Saskatoon, SK, S7N 5C9, Canada. *e-mail: tim.kelly@usask.ca

Figure 1 | Device architecture and energy-level diagram. a, Device architecture of the ITO/ZnO/CH$_3$NH$_3$PbI$_3$/spiro-OMeTAD/Ag cells tested in this study. **b**, Energy levels (relative to vacuum) of the various device components.

the thickness of which can be varied systematically by repeating the spin-coating process several times. A two-step process was then used to grow the CH$_3$NH$_3$PbI$_3$ layer[21]. This consisted of spin coating a layer of PbI$_2$ onto the ZnO surface, followed by immersion of the substrate in a solution of CH$_3$NH$_3$I. The efficiency of the subsequent devices was found to vary with CH$_3$NH$_3$I concentration, solution temperature and dipping time, and care was taken to ensure that the processing conditions were reproduced as consistently as possible. Spin coating of the spiro-OMeTAD hole-transport material and thermal evaporation of the Ag top contact completes the device structure (Fig. 1a). The CH$_3$NH$_3$PbI$_3$ perovskite is a direct, low-bandgap semiconductor with good carrier mobility; based on the relative energy levels of the various device components (Fig. 1b), free charge carriers (or excitons) generated in the CH$_3$NH$_3$PbI$_3$ layer can be extracted (or dissociated) by either transferring an electron to the underlying ZnO layer, or through hole transfer to the spiro-OMeTAD hole-transport material. Given the highly selective nature of both the ZnO and spiro-OMeTAD layers, this is expected to lead to highly efficient devices with good fill factors.

To probe the effect of ZnO layer thickness on device performance, devices were prepared by spin coating zero, one, three, five and eight layers of ZnO nanoparticles (Table 1). This produced electron-transport layers that varied from 0 to 70 nm in thickness. As can be seen from the data, the presence of an efficient electron-transport layer is crucial to obtain high-performance devices. Without the ZnO layer, the fill factor and open-circuit voltage (V_{oc}) are very low because of increased recombination at the ITO surface and a correspondingly low shunt resistance. Incorporating even a very thin (10 nm) ZnO layer into the device substantially improves both the V_{oc} and the fill factor, and for a ZnO thickness of 25 nm, PCEs in excess of 14% were obtained. Further increases

in the thickness of the ZnO layer did not result in any improvements in device performance.

To ensure the reproducibility of the results, over 100 separate devices were fabricated and tested using the optimized ZnO thickness of 25 nm. Histograms of the cell-performance characteristics are shown in Fig. 2, and the average device parameters are tabulated in Supplementary Table 1. As can be seen from the results, the devices performed extremely well. The V_{oc} values were highly reproducible and in excess of 1.0 V, and the average short-circuit current density (J_{sc}) was nearly 20 mA cm^{-2}. When combined with the very good fill factors (>70%), this produced an average PCE of 13.7%. Both the reproducibility of the device fabrication procedure (a 7.6% relative standard deviation in PCE) and the excellent PCEs are highly encouraging. Clearly, both our results and those of Liu et al.[29] indicate that the mesoporous scaffolds utilized in other device architectures are superfluous for the production of high-performance cells. Furthermore, not only is the average PCE reported here (13.7%) substantially higher than the equivalent average PCE for solution-processed planar-junction devices reported in the literature (≤9%)[29,30], but also it is noticeably higher than even those devices constructed using high-vacuum vapour-phase deposition techniques (12.3%)[29].

The current–voltage (J–V) characteristics and incident photon-to-current efficiency (IPCE) spectrum of the highest-performing device is shown in Fig. 3. From the J–V curve measured under standard AM1.5G illumination, the J_{sc}, V_{oc}, fill factor and PCE were determined as 20.4 mA cm^{-2}, 1.03 V, 74.9% and 15.7%, respectively. The very high PCE of 15.7% makes this device one of the highest-performing solution-processed cells reported to date, which is especially remarkable given the complete lack of a mesoporous scaffold and any high-temperature processing steps. The IPCE spectrum shows the expected behaviour for a high-performance device based on CH$_3$NH$_3$PbI$_3$. The onset of photocurrent at 800 nm is consistent with the reported bandgap of CH$_3$NH$_3$PbI$_3$ (ref. 34), and the efficiency of 75–80% obtained across almost the entire spectrum (360–750 nm) highlights the excellent performance of the device. Based on the absorption spectrum of a representative CH$_3$NH$_3$PbI$_3$ film (Supplementary Fig. 2), the light-harvesting efficiency of the devices is estimated to be >95% below 650 nm and ~85% between 650 and 750 nm, which implies a high internal quantum efficiency (absorbed photon-to-current efficiency). Integrating the product of the AM1.5G photon flux with the

Table 1 | Device parameters for solar cells prepared with varying thicknesses of ZnO.

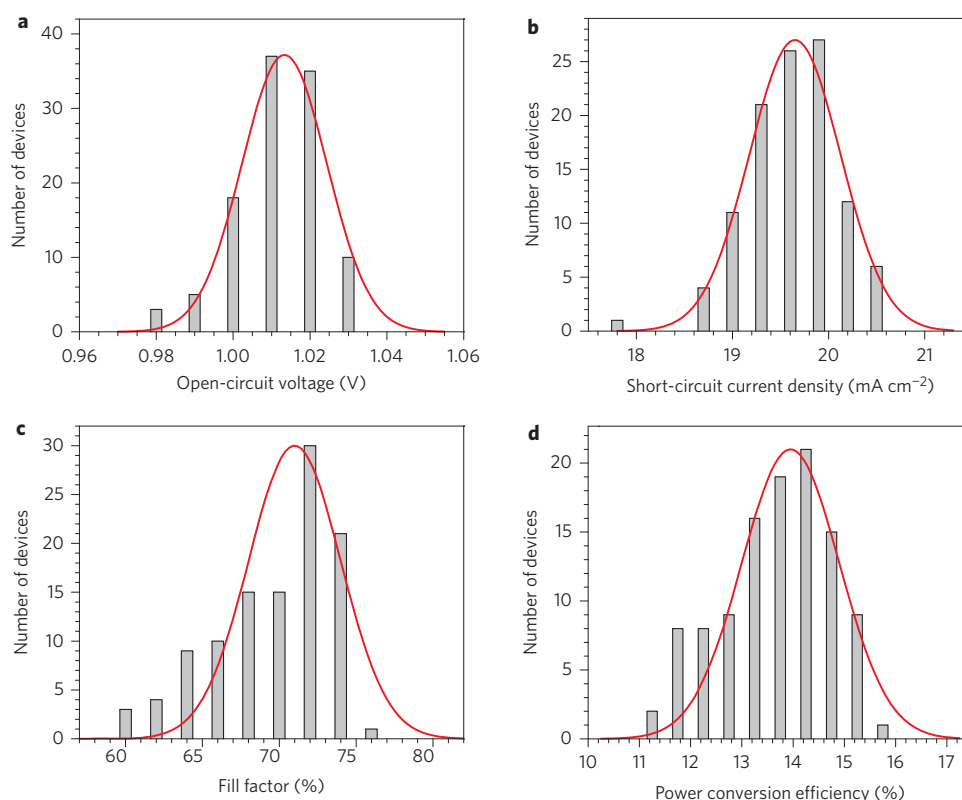| No. of layers	ZnO thickness (nm)	J_{sc} (mA cm^{-2})	V_{oc} (V)	Fill factor (%)	PCE (%)
0	0	16.5	0.46	31.7	2.4
1	10	18.0	0.99	62.4	11.1
3	25	20.5	1.01	69.6	14.4
5	40	18.9	1.01	70.0	13.3
8	70	18.4	1.01	69.5	12.9

Figure 2 | Histograms of device parameters measured for 108 separate ITO/ZnO/CH$_3$NH$_3$PbI$_3$/spiro-OMeTAD/Ag devices. a–d, V_{oc} (**a**), J_{sc} (**b**), fill factor (**c**) and PCE (**d**). The Gaussian fits are provided as a guide to the eye.
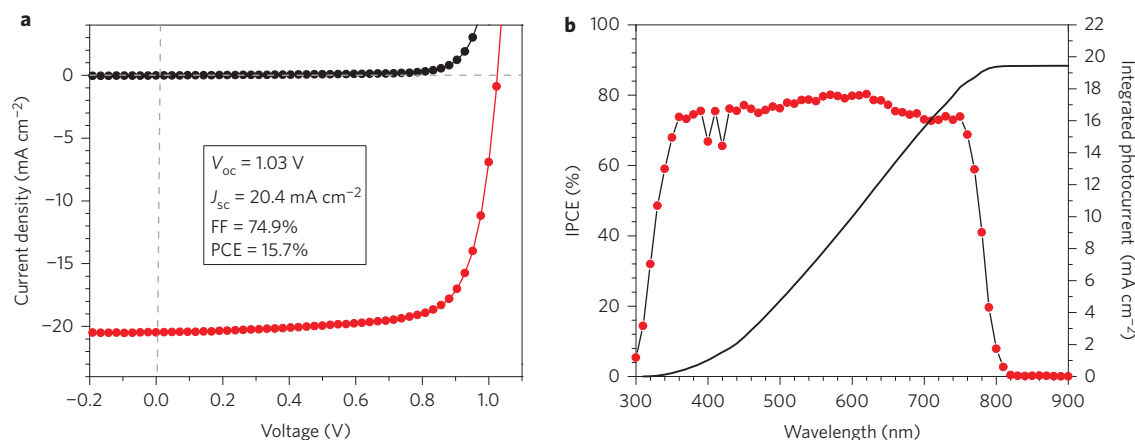

Figure 3 | J–V curves and IPCE spectrum of the highest-performing device in this study. a, J–V characteristics measured under 100 mW cm^{-2} AM1.5G illumination (red line) and in the dark (black line) for the highest-performing ITO/ZnO/CH$_3$NH$_3$PbI$_3$/spiro-OMeTAD/Ag device. **b,** IPCE spectrum of the highest-performing ITO/ZnO/CH$_3$NH$_3$PbI$_3$/spiro-OMeTAD/Ag device (red circles). The integrated product of the IPCE spectrum with the AM1.5G photon flux is also shown (black line).

IPCE spectrum yields a predicted J_{sc} of 19.4 mA cm^{-2}, which is in agreement with the measured value of 20.4 mA cm^{-2}.

The origin of the high performances observed in the ITO/ZnO/CH$_3$NH$_3$PbI$_3$/spiro-OMeTAD/Ag devices was investigated further by studying the morphologies of the various layers of the device stack. Although the relative proportion of photogenerated free-charge carriers versus excitons is unknown, previous reports proposed that charge extraction and/or exciton dissociation occurs predominantly at the mesoporous TiO$_2$/CH$_3$NH$_3$PbI$_3$ interface[20,21]. However, the ZnO nanoparticle film utilized in the current study is quite compact, with little surface roughness or porosity visible under the scanning electron microscope (SEM; see

Supplementary Fig. 3). As such, the cells prepared in this study more closely resemble those of Liu et al.[29], in which a compact TiO$_2$ layer served as the electron-selective contact; in these cells, there is also very limited interfacial surface area between the electron-selective contact and the perovskite absorber. Given the high efficiencies of both our devices and the planar heterojunctions of Liu et al.[29], carrier collection at the ZnO/CH$_3$NH$_3$PbI$_3$ interface clearly does not limit the overall photocurrent. In the case of the planar heterojunctions, this can be understood on the basis of the very long electron–hole diffusion lengths of the mixed halide CH$_3$NH$_3$PbI$_{3-x}$Cl$_x$ perovskites employed (on the order of 1 μm)[35]; as the diffusion lengths are substantially greater than the absorption
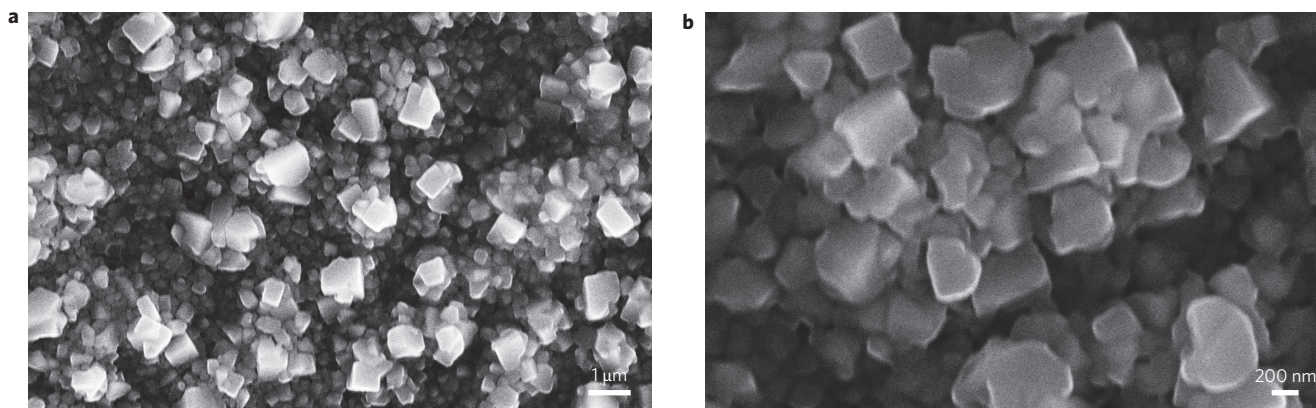
Figure 4 | SEM micrographs of the ITO/ZnO/CH$_3$NH$_3$PbI$_3$ film. a, Low-magnification SEM micrograph of the surface of the ITO/ZnO/CH$_3$NH$_3$PbI$_3$ film. **b**, High-magnification SEM micrograph of the surface of the ITO/ZnO/CH$_3$NH$_3$PbI$_3$ film.

depth of the material, the planar heterojunction structure does not affect the PCE detrimentally. In contrast, for the pure iodide-based perovskite used in the present work, the electron–hole diffusion lengths are only on the order of 100 nm (refs 35,36), which is substantially lower than the CH$_3$NH$_3$PbI$_3$ film thickness ($\sim$300 nm). Therefore, the interfacial surface area between the perovskite and the hole-transport material is of substantial importance. The surface of the ITO/ZnO/CH$_3$NH$_3$PbI$_3$ layer is shown in Fig. 4, which reveals the formation of large (100–1,000 nm) crystallites of CH$_3$NH$_3$PbI$_3$ that were not present in the PbI$_2$ precursor film (Supplementary Fig. 4).

We propose that in the absence of a mesoporous scaffold, perovskite crystal growth is relatively unconstrained during the immersion of the PbI$_2$-coated film in the CH$_3$NH$_3$I solution. This is supported by powder X-ray diffraction measurements (Supplementary Fig. 5). The data are consistent with the tetragonal phase of CH$_3$NH$_3$PbI$_3$ (ref. 34) and, most importantly, the relative sharpness of the peaks is indicative of the large crystallite size. Analysis of the peak full-width-half-maxima via the Debye–Scherrer equation provides an estimated crystallite size of 75 nm. Given that this represents a lower bound on the crystallite size, the data are in quite reasonable agreement with the smaller particles observed in the SEM images. The increased crystallite size results in a highly roughened CH$_3$NH$_3$PbI$_3$/spiro-OMeTAD interface; importantly, the crystallite size is commensurate with the electron–hole diffusion lengths in CH$_3$NH$_3$PbI$_3$, and thus ensures a high level of carrier extraction from the perovskite film. The large crystallite size may also serve to increase the carrier mobility within the CH$_3$NH$_3$PbI$_3$ layer and reduce recombination from defect and trap states. These factors, at least in part, explain the high J_{sc} values and fill factors observed in the present study; however, to achieve the very high J_{sc} values of the highest-performing cells ($>$20 mA cm^{-2}), additional factors must also be considered. Previous reports of CH$_3$NH$_3$PbI$_3$-based cells all focused on the use of compact TiO$_2$ electron-transport layers[21,25,29,30]; however, many studies show that ZnO has a substantially higher electron mobility than TiO$_2$ (ref. 31). The higher electron mobility may help contribute to the observed increase in J_{sc}. Additionally, the large crystallites observed at the surface of the CH$_3$NH$_3$PbI$_3$ layer act as scattering centres for the incoming light, which efficiently re-directs it off-normal and thereby increases the effective optical path length of the device. The non-zero absorbance at sub-bandgap wavelengths (800 nm) in Supplementary Fig. 2 is consistent with scattering from the CH$_3$NH$_3$PbI$_3$ film. The contributions of all of these factors (efficient carrier collection and/or exciton dissociation, improved mobility within the electron-transport layer and extensive light scattering) probably give rise to the high photocurrents that are observed.

One of the main advantages in the use of the ZnO nanoparticle layer is that no sintering or annealing step is required. The other major fabrication steps (spin coating of PbI$_2$, soaking in CH$_3$NH$_3$I solution and spin coating of spiro-OMeTAD) are also carried out by solution-processing techniques at room temperature, which means this fabrication process is ideal for the preparation of devices on flexible substrates. The ITO/glass substrate was therefore replaced with thin films of ITO/poly(ethylene terephthalate) (PET), and a number of devices were fabricated using the same preparation procedures. The results of this study are shown in Fig. 5.

As can be seen from Fig. 5, the devices on ITO/PET substrates performed reasonably well. The J–V curve of the highest-performing device on a flexible substrate is shown in Fig. 5a, which yields a V_{oc} of 1.03 V, a J_{sc} of 13.4 mA cm^{-2}, a fill factor of 73.9% and a PCE of 10.2%. Although lower than the efficiency of devices fabricated on ITO/glass substrates (primarily because of the lower J_{sc}), the successful combination of device flexibility and a PCE $>$ 10% is highly promising. Some insight into the lower J_{sc} can be gained from the IPCE spectrum (Fig. 5b). In contrast to the broad, flat IPCE spectrum observed on rigid substrates (Fig. 3b), the IPCE spectrum of the device fabricated on PET displays a broad peak at 450 nm with a pronounced shoulder at 680 nm. This leads to a substantial loss of photocurrent in the 500–800 nm range, as compared to the devices fabricated on glass. Bending tests show that the device performs well even after being bent repeatedly to decreasing radii of curvature (Fig. 5d). We decreased the radius of curvature to the point where the ITO/PET substrate could no longer recover its shape and observed less than a 15% drop in efficiency. Importantly, our results suggest that the flexibility of the device is limited by the flexibility of the ITO/PET substrate, and not by the perovskite layer. Therefore, although the flexible devices have lower efficiencies than those prepared on rigid substrates, this is a substantial step forward in the development of hybrid organic–inorganic solar cells. Flexible devices are especially attractive for a variety of consumer-driven applications, such as power-generating fabrics, clothing and textiles[37]. To the best of our knowledge, there is only one other report of a flexible perovskite solar cell[38], and no reports of a flexible perovskite device with a PCE over 10%.

We have developed ZnO nanoparticle electron-transport layers for CH$_3$NH$_3$PbI$_3$-based solar cells, and demonstrated that neither a mesoporous scaffold nor any high-temperature processing steps are required to achieve PCEs as high as 15.7%. This is expected to simplify dramatically the device fabrication procedures for such devices, but at the same time maintain or improve their already-high device efficiency. The high performance of these cells
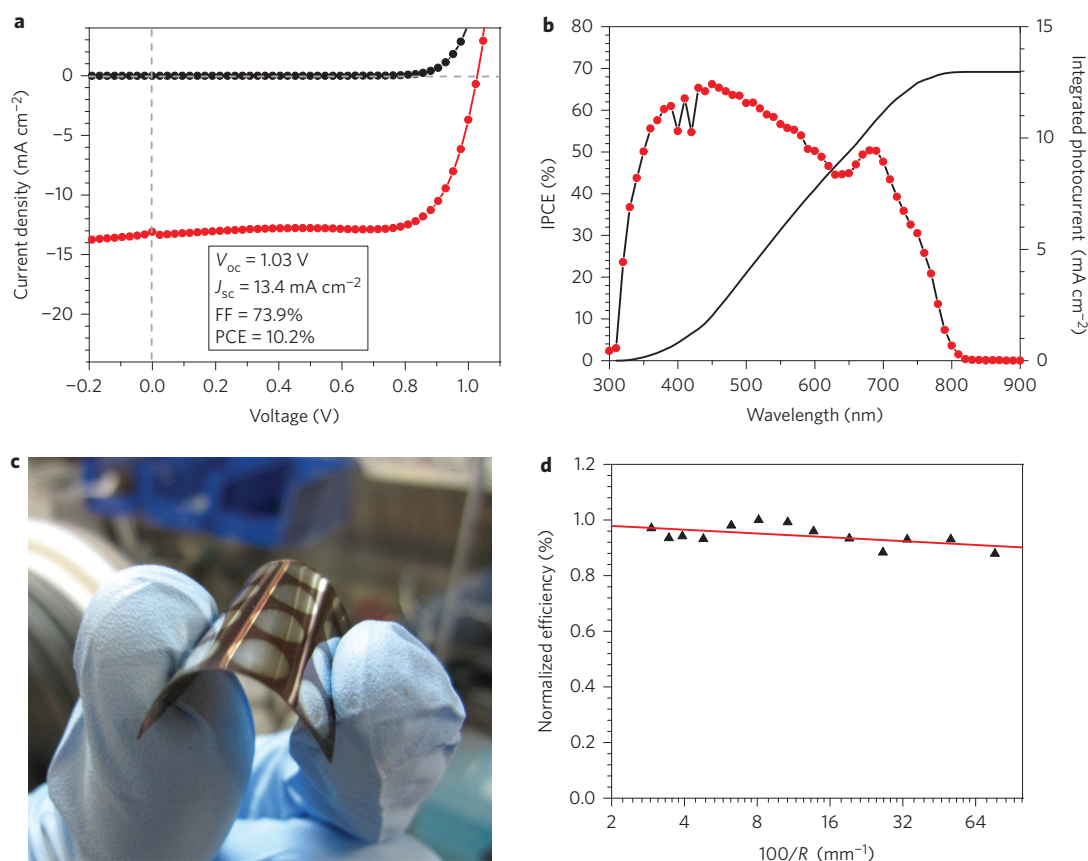
Figure 5 | Device performance, IPCE spectrum, photograph and bending tests for a device prepared on a flexible PET substrate. a, J–V characteristics measured under 100 mW cm^{-2} AM1.5G illumination (red line) and in the dark (black line) for the highest-performing ITO/ZnO/CH$_3$NH$_3$PbI$_3$/spiro-OMeTAD/Ag flexible device. **b,** IPCE spectrum of the highest-performing ITO/ZnO/CH$_3$NH$_3$PbI$_3$/spiro-OMeTAD/Ag flexible device (red circles). The integrated product of the IPCE spectrum with the AM1.5G photon flux is also shown (black line). **c,** Photograph of an ITO/ZnO/CH$_3$NH$_3$PbI$_3$/spiro-OMeTAD/Ag device prepared on a flexible PET substrate. **d,** Normalized PCE (measured on a flat device) after first bending the substrate around a cylindrical object of the specified radius (R). All measurements were performed on a single device and were measured from the highest to the lowest radius of curvature. The linear fit is provided as a guide to the eye.

appears to originate from the unconstrained crystallite growth that occurs in the absence of a mesoporous scaffold. Large crystallites of CH$_3$NH$_3$PbI$_3$ lead to a highly textured CH$_3$NH$_3$PbI$_3$/spiro-OMeTAD interface, the dimensions of which are commensurate with the electron–hole diffusion lengths. The crystallites also act as efficient light scattering centres, which increases the effective optical path length of the device. The combination of these effects leads to values of J_{sc} greater than 20 mA cm^{-2}. Flexible devices on ITO/PET substrates can also be prepared by this route, and display PCEs in excess of 10%. This combination of ease-of-fabrication, room-temperature processing, high device performance and device flexibility are all expected to help push these hybrid organic–inorganic solar cells closer to commercial viability.

Note added in proof: During the revision of this paper, a highly relevant article to this topic was published: P. Docampo, J.M. Ball, M. Darwich, G.E. Eperon, & H.J. Snaith, Efficient organometal trihalide perovskite planar-heterojunction solar cells on flexible polymer substrates. *Nature Commun.* **4**, 2761 (2013).

Methods

Synthesis of ZnO nanoparticles. ZnO nanoparticles were prepared according to literature procedures[32,33]. Zinc acetate dihydrate (2.95 g, 13.4 mmol) was dissolved in methanol (125 ml) with stirring at 65 °C. A solution of KOH (1.48 g, 23 mmol) in methanol (65 ml) was then added dropwise at 60–65 °C over a period of 15 min. The reaction mixture was stirred for 2.5 h at 65 °C. After cooling to room temperature, the supernatant was decanted and the precipitate washed twice with methanol

(20 ml). *n*-butanol (70 ml), methanol (5 ml) and chloroform (5 ml) were added to disperse the precipitate and produce a ZnO nanoparticle solution with a concentration of 6 mg ml^{-1}. Before use, the ZnO nanoparticle solution was filtered through a 0.45 μm PVDF syringe filter.

Solar cell fabrication. Solar cells were fabricated on precleaned ITO-coated glass substrates with a sheet resistance of 20 Ω sq^{-1}. First, a thin ZnO nanoparticle layer was spin coated onto the substrate at 3,000 r.p.m. for 30 s. The procedure was repeated three times to obtain a continuous smooth film. A PbI$_2$ solution (dissolved in *N,N*-dimethylformamide at a concentration of 460 mg ml^{-1}) was then spin coated on top of the ZnO layer at 3,000 r.p.m. for 15 s. After drying for several minutes in air, the substrate was dipped into a solution of CH$_3$NH$_3$I in 2-propanol (10 mg ml^{-1}) for 40 s, then dried under a flow of clean air. Subsequently, the spiro-OMeTAD-based hole-transfer layer (80 mg spiro-OMeTAD, 28.5 μl 4-*tert*-butylpyridine and 17.5 μl lithium-bis(trifluoromethanesulfonyl)imide (Li-TFSI) solution (520 mg Li-TFSI in 1 ml acetonitrile) all dissolved in 1 ml chlorobenzene) was deposited by spin coating at 4,000 r.p.m. for 30 s. Finally, a 150-nm-thick silver layer was deposited by thermal evaporation at a base pressure of 2 × 10^{-6} mbar. The completed devices were stored in a N$_2$-purged glovebox (<0.1 ppm O$_2$ and H$_2$O). Prior to the evaporation of the Ag top contact, all device fabrication steps were carried out under ambient conditions.

Device characterization. The current–voltage curves of solar cells were measured inside the glovebox using a Keithley 2400 source-measure unit. The cells were illuminated by a 450 W Class AAA solar simulator equipped with an AM1.5G filter (Sol3A, Oriel Instruments) at a calibrated intensity of 100 mW cm^{-2}, as determined by a standard silicon reference cell (91150V, Oriel Instruments). The effective area of the cell was defined as 0.07065 cm^2 using a non-reflective metal mask. IPCE spectra were measured in air using a commercial IPCE set-up (QE-PV-Si, Oriel Instruments). Monochromated light was chopped at a frequency of 8 Hz and photocurrents measured using a lock-in amplifier.

References

1. Park, S. H. *et al.* Bulk heterojunction solar cells with internal quantum efficiency approaching 100%. *Nature Photon.* **3,** 297–302 (2009).
2. Chen, H-Y. *et al.* Polymer solar cells with enhanced open-circuit voltage and efficiency. *Nature Photon.* **3,** 649–653 (2009).
3. Guo, X. *et al.* Polymer solar cells with enhanced fill factors. *Nature Photon.* **7,** 825–833 (2013).
4. Hardin, B. E., Snaith, H. J. & McGehee, M. D. The renaissance of dye-sensitized solar cells. *Nature Photon.* **6,** 162–169 (2012).
5. Yella, A. *et al.* Porphyrin-sensitized solar cells with cobalt (II/III)-based redox electrolyte exceed 12 percent efficiency. *Science* **334,** 629–634 (2011).
6. Park, N-G. Organometal perovskite light absorbers toward a 20% efficiency low-cost solid-state mesoscopic solar cell. *J. Phys. Chem. Lett.* **4,** 2423–2429 (2013).
7. Kojima, A., Teshima, K., Shirai, Y. & Miyasaka, T. Organometal halide perovskites as visible-light sensitizers for photovoltaic cells. *J. Am. Chem. Soc.* **131,** 6050–6051 (2009).
8. Zhao, Y. & Zhu, K. Charge transport and recombination in perovskite $(CH_3NH_3)PbI_3$ sensitized TiO_2 solar cells. *J. Phys. Chem. Lett.* **4,** 2880–2884 (2013).
9. Im, J-H., Lee, C-R., Lee, J-W., Park, S-W. & Park, N-G. 6.5% efficient perovskite quantum-dot-sensitized solar cell. *Nanoscale* **3,** 4088–4093 (2011).
10. Noh, J. H. *et al.* Nanostructured $TiO_2/CH_3NH_3PbI_3$ heterojunction solar cells employing spiro-OMeTAD/Co-complex as hole-transporting material. *J. Mater. Chem. A* **1,** 11842–11847 (2013).
11. Kim, H-S. *et al.* Lead iodide perovskite sensitized all-solid-state submicron thin film mesoscopic solar cell with efficiency exceeding 9%. *Sci. Rep.* **2,** 591 (2012).
12. Chung, I., Lee, B., He, J., Chang, R. P. H. & Kanatzidis, M. G. All-solid-state dye-sensitized solar cells with high efficiency. *Nature* **485,** 486–489 (2012).
13. Etgar, L. *et al.* Mesoscopic $CH_3NH_3PbI_3/TiO_2$ heterojunction solar cells. *J. Am. Chem. Soc.* **134,** 17396–17399 (2012).
14. Edri, E., Kirmayer, S., Cahen, D. & Hodes, G. High open-circuit voltage solar cells based on organic–inorganic lead bromide perovskite. *J. Phys. Chem. Lett.* **4,** 897–902 (2013).
15. Im, J-H., Chung, J., Kim, S-J. & Park, N-G. Synthesis, structure, and photovoltaic property of a nanocrystalline 2H perovskite-type novel sensitizer $(CH_3CH_2NH_3)PbI_3$. *Nanoscale Res. Lett.* **7,** 353–359 (2012).
16. Noh, J. H., Im, S. H., Heo, J. H., Mandal, T. N. & Seok, S. I. Chemical management for colorful, efficient, and stable inorganic–organic hybrid nanostructured solar cells. *Nano Lett.* **13,** 1764–1769 (2013).
17. Cai, B., Xing, Y., Yang, Z., Zhang, W-H. & Qiu, J. High performance hybrid solar cells sensitized by organolead halide perovskites. *Energy Environ. Sci.* **6,** 1480–1485 (2013).
18. Qiu, J. *et al.* All-solid-state hybrid solar cells based on a new organometal halide perovskite sensitizer and one-dimensional TiO_2 nanowire arrays. *Nanoscale* **5,** 3245–3248 (2013).
19. Bi, D., Yang, L., Boschloo, G., Hagfeldt, A. & Johansson, E. M. J. Effect of different hole transport materials on recombination in $CH_3NH_3PbI_3$ perovskite-sensitized mesoscopic solar cells. *J. Phys. Chem. Lett.* **4,** 1532–1536 (2013).
20. Heo, J. H. *et al.* Efficient inorganic–organic hybrid heterojunction solar cells containing perovskite compound and polymeric hole conductors. *Nature Photon.* **7,** 486–491 (2013).
21. Burschka, J. *et al.* Sequential deposition as a route to high-performance perovskite-sensitized solar cells. *Nature* **499,** 316–319 (2013).
22. McGehee, M. D. Materials science: fast-track solar cells. *Nature* **501,** 323–325 (2013).
23. Boix, P. P. *et al.* Role of ZnO electron-selective layers in regular and inverted bulk heterojunction solar cells. *J. Phys. Chem. Lett.* **2,** 407–411 (2011).
24. Ha, Y. E. *et al.* Inverted type polymer solar cells with self-assembled monolayer treated ZnO. *J. Phys. Chem. C* **117,** 2646–2652 (2013).
25. Lee, M. M., Teuscher, J., Miyasaka, T., Murakami, T. N. & Snaith, H. J. Efficient hybrid solar cells based on meso-superstructured organometal halide perovskites. *Science* **338,** 643–647 (2012).
26. Zhang, W. *et al.* Enhancement of perovskite-based solar cells employing core–shell metal nanoparticles. *Nano Lett.* **13,** 4505–4510 (2013).
27. Ball, J. M., Lee, M. M., Hey, A. & Snaith, H. J. Low-temperature processed meso-superstructured to thin-film perovskite solar cells. *Energy Environ. Sci.* **6,** 1739–1743 (2013).
28. Carnie, M. J. *et al.* A one-step low temperature processing route for organolead halide perovskite solar cells. *Chem. Commun.* **49,** 7893–7895 (2013).
29. Liu, M., Johnston, M. B. & Snaith, H. J. Efficient planar heterojunction perovskite solar cells by vapour deposition. *Nature* **501,** 395–398 (2013).
30. Eperon, G. E., Burlakov, V. M., Docampo, P., Goriely, A. & Snaith, H. J. Morphological control for high performance, solution-processed planar heterojunction perovskite solar cells. *Adv. Funct. Mater.* http://dx.doi.org/10.1002/adfm.201302090.
31. Zhang, Q., Dandeneau, C. S., Zhou, X. & Cao, G. ZnO nanostructures for dye-sensitized solar cells. *Adv. Mater.* **21,** 4087–4108 (2009).
32. Beek, W. J. E., Wienk, M. M., Kemerink, M., Yang, X. & Janssen, R. A. J. Hybrid zinc oxide conjugated polymer bulk heterojunction solar cells. *J. Phys. Chem. B* **109,** 9505–9516 (2005).
33. Pacholski, C., Kornowski, A. & Weller, H. Self-assembly of ZnO: from nanodots to nanorods. *Angew. Chem. Int. Ed.* **41,** 1188–1191 (2002).
34. Baikie, T. *et al.* Synthesis and crystal chemistry of the hybrid perovskite $(CH_3NH_3)PbI_3$ for solid-state sensitised solar cell applications. *J. Mater. Chem. A* **1,** 5628–5641 (2013).
35. Stranks, S. D. *et al.* Electron-hole diffusion lengths exceeding 1 micrometer in an organometal trihalide perovskite absorber. *Science* **342,** 341–344 (2013).
36. Xing, G. *et al.* Long-range balanced electron- and hole-transport lengths in organic–inorganic $CH_3NH_3PbI_3$. *Science* **342,** 344–347 (2013).
37. Kaltenbrunner, M. *et al.* Ultrathin and lightweight organic solar cells with high flexibility. *Nature Commun.* **3,** 770 (2012).
38. Kumar, M. H. *et al.* Flexible, low-temperature, solution processed ZnO-based perovskite solid state solar cells. *Chem. Commun.* **49,** 11089–11091 (2013).

Acknowledgements

Author contributions

D.L. carried out the device fabrication and performance measurements. T.L.K. prepared the manuscript and directed the study. Both D.L. and T.L.K. conceived the experiments, and contributed to data analysis, the discussion of the results and manuscript revisions.

Additional information

Supplementary information is available in the online version of the paper. Reprints and permissions information is available online at www.nature.com/reprints. Correspondence and requests for materials should be addressed to T.L.K.

Competing financial interests

D.L. and T.K. are named inventors on US provisional patent application 61/891,020 (filing date 15.10.2013), which is related to the techniques described in this article.